Record-Breaking Summer Rainfall in South Korea in 2020: Synoptic Characteristics and the Role of Large-Scale Circulations

CHANIL PARK,[a] SEOK-WOO SON,[a] HERA KIM,[a] YOO-GEUN HAM,[b] JOOWAN KIM,[c] DONG-HYUN CHA,[d] EUN-CHUL CHANG,[c] GYUWON LEE,[e] JONG-SEONG KUG,[f] WOO-SEOP LEE,[g] YUN-YOUNG LEE,[g] HEE CHOON LEE,[h] AND BYUNGHWAN LIM[h]

[a] *School of Earth and Environmental Sciences, Seoul National University, Seoul, South Korea*
[b] *Department of Oceanography, Chonnam National University, Gwangju, South Korea*
[c] *Department of Atmospheric Sciences, Kongju National University, Kongju, South Korea*
[d] *School of Urban and Environmental Engineering, Ulsan National Institute of Science and Technology, Ulsan, South Korea*
[e] *Department of Astronomy and Atmospheric Sciences, Center for Atmospheric REmote sensing (CARE), Kyungpook National University, Daegu, South Korea*
[f] *Division of Environmental Science and Engineering, Pohang University of Science and Technology, Pohang, South Korea*
[g] *Climate Services and Research Division, APEC Climate Center, Busan, South Korea*
[h] *National Institute of Meteorological Sciences, Jeju, South Korea*

(Manuscript received 17 March 2021, in final form 16 June 2021)

ABSTRACT: In the summer of 2020, South Korea experienced record-breaking rainfall due to 15 consecutive heavy rainfall events (HREs) from mid-June to early September. Among them, 11 HREs occurred in late June to mid-August with distinct synoptic characteristics depending on the occurrence period. All HREs from 29 June to 27 July (P1) were triggered by extratropical cyclones, while those from 28 July to 15 August (P2) mainly occurred along the monsoon rainband. We argue that their transition is associated with atmospheric teleconnections. During P1, the western North Pacific subtropical high (WNPSH) anomalously extended westward, but its northward expansion was hindered by the meridional wave train from the suppressed convection over the South China Sea. This condition prevented a northward migration of the monsoon rainband but allowed more extratropical cyclones to pass over the Korean Peninsula, resulting in four HREs. During P2, the South China Sea convection was enhanced, and its circulation response prompted an abrupt northward expansion of the WNPSH with a large pressure gradient along its northern boundary. With intensified southwesterly moisture transport, a monsoon rainband was activated over the Korean Peninsula, producing six HREs. The opposite phases of the summer North Atlantic Oscillation, i.e., negative in P1 but positive in P2, further contributed to the anomalous monsoon circulation by modulating the midlatitude circulation response to the South China Sea convection. This study demonstrates that the nature of summertime HREs in East Asia can be strongly modulated by remote forcings.

KEYWORDS: Extreme events; Rainfall; Monsoons; Synoptic-scale processes; Teleconnections

1. Introduction

In the summer of 2020, destructive floods consecutively occurred across South Korea, causing 46 fatalities and billion-dollar economic losses [Korea Meteorological Administration (KMA) 2021]. The accumulated rainfall during June–September was approximately 53% larger than climatology, breaking the record since 1971 (Fig. 1a). This extreme summer rainfall was primarily attributed to consecutive heavy rainfall events (HREs) from mid-June to early September. A large number of flash floods were also reported in China in June–July and Japan in early July (Liu et al. 2020; Takaya et al. 2020; Araki et al. 2021; Horinouchi et al. 2021; Zhang et al. 2021; Zhou et al. 2021). This indicates that the HREs in South Korea were not local phenomena but a regional manifestation of an abnormal East Asian summer monsoon (EASM) in 2020.

The present study documents the synoptic characteristics of the HREs in South Korea. The anomalous EASM circulation and its possible causes are also examined. Although several studies have already reported hydrological extremes in East Asia in 2020 summer (referenced above), no study has reported South Korean HREs that were not necessarily driven by the same mechanisms as in the Chinese or Japanese HREs. As shown below, South Korean HREs exhibited distinct synoptic characteristics depending on the occurrence period, which are distinguishable from Chinese or Japanese HREs.

In recent decades, many catastrophic HREs have occurred in East Asia. For example, an exceptionally serious flood occurred along the Yangtze River due to three consecutive HREs on 11–29 June, 21–31 July, and 1–10 August 1998 (Xiong et al. 2003). In South Korea, the 18-day lasting HRE, resulting from the vertical coupling of persistent low-level and upper-level jets, caused the flash flood in August 1998 (Choi et al. 2008; Lee et al. 2008). In western Japan, extreme rainfall in excess of 100 mm h^{-1} caused 75 deaths in August 2014 due to the interplay between the elongated water vapor flux (known as the

Supplemental information related to this paper is available at the Journals Online website: https://doi.org/10.1175/MWR-D-21-0051.s1

Corresponding author: Seok-Woo Son, seokwooson@snu.ac.kr

DOI: 10.1175/MWR-D-21-0051.1

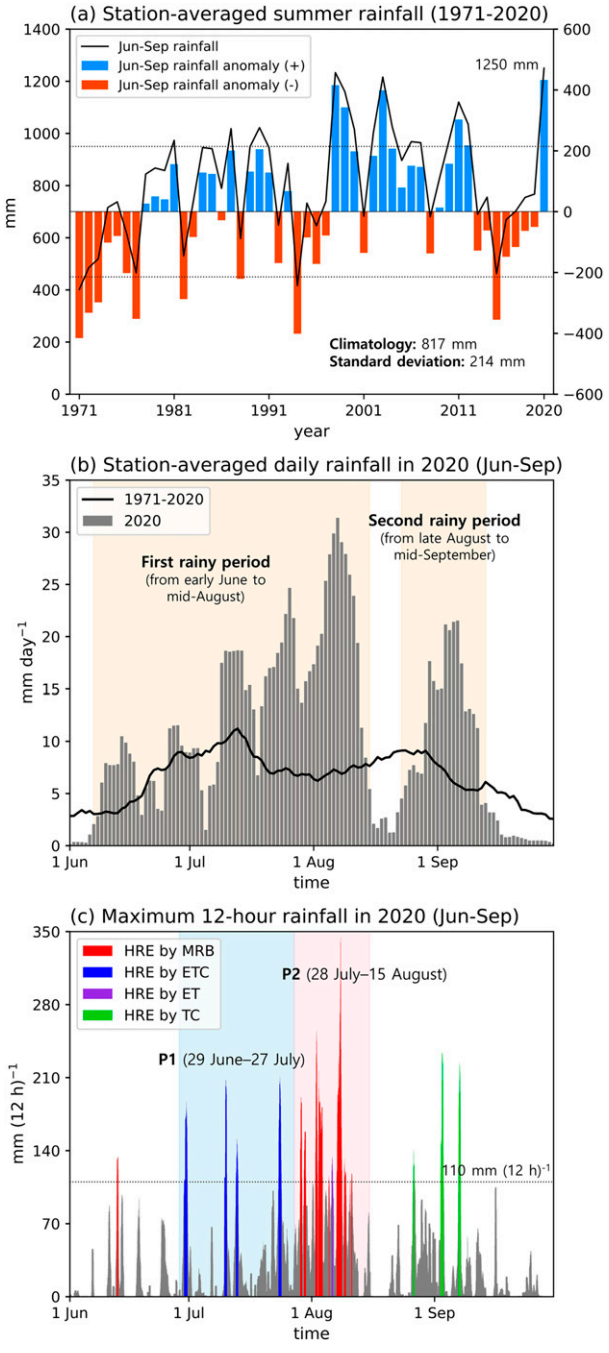

FIG. 1. (a) Yearly time series of June–September accumulated rainfall (black line) and its anomaly (colored bars) for the period of 1971–2020. Here, the anomaly is defined as a deviation from the 50-yr (1971–2020) climatology, and its one standard deviation is marked by dotted lines. (b) Daily time series of daily accumulated rainfall amount in the summer of 2020 (gray bars) and the 50-yr climatology (black line). A 9-day moving average is applied. The first and second rainy periods in 2020 are denoted by apricot shading. In (a) and (b), the accumulated rainfall amounts are averaged over 45 stations with continuous observations from 1971 to 2020. (c) Hourly time series of the 12-h accumulated rainfall amounts in the summer of 2020. Rainfall amounts greater than 110 mm $(12\ h)^{-1}$ are highlighted in four different colors depending on their associated synoptic systems, i.e., monsoon rainband (MRB), extratropical cyclone (ETC), extratropical transition (ET), and tropical cyclone (TC). In (c), the maximum rainfall amounts among 91 stations operated in 2020 are shown. The areas shaded in sky-blue and pink denote P1 (29 Jun–27 Jul) and P2 (28 Jul–15 Aug), respectively.

"atmospheric river") and the upper-level cutoff low (Hirota et al. 2016). In July 2018, western Japan again experienced a severe HRE due to a localized rainband, which was activated by continuous low-level moisture supply and an upper-level deep trough (Yokoyama et al. 2020).

Beyond these case studies, the overall synoptic characteristics of the summertime HREs (more generally, monsoon rainfall) in East Asia have been extensively examined. It is well documented that East Asian HREs typically develop through warm cloud processes supported by abundant moisture supply along the northern flank of the western North Pacific subtropical high (WNPSH; Sohn et al. 2013; Hamada and Takayabu 2018). This moisture supply is frequently driven into an elongated shape, i.e., atmospheric river (Kamae et al. 2017; Park et al. 2021a). Sampe and Xie (2010) further showed that westerly warm advection in the midtroposphere provides an environmental forcing for the ascending motion along the quasi-stationary monsoon rainband (MRB). By analyzing the 350-K isentropic potential vorticity (PV) map, Horinouchi (2014) demonstrated that monsoon rainfall can be transiently modulated by upper-level disturbances. The mixture of thermodynamic and dynamic natures of the East Asian HREs is also well supported by observational studies on the HREs in eastern China (Nie and Fan 2019), Korea (Park et al. 2021b) and Japan (Yokoyama et al. 2020). They all demonstrated that the summertime HREs in East Asia are governed by synoptic-scale setup, although the rainfall itself tends to be localized (Jo et al. 2020).

The synoptic condition of the EASM can be influenced by remote forcings through atmospheric teleconnections. For example, the enhanced convection over the warm tropical Indian Ocean in the post–El Niño summer often leads to the increased monsoon southwesterly toward East Asia by organizing an anomalous anticyclone over the subtropical western North Pacific (Xie et al. 2009, 2016). A meridional propagation of the Rossby wave excited by convection over the South China Sea (SCS), known as the Pacific–Japan (PJ) pattern (Nitta 1987; Kosaka and Nakamura 2006), can also drive abnormal behaviors of the WNPSH on intraseasonal to interannual time scales (Kosaka et al. 2011; Li et al. 2014; Kubota et al. 2016).

The extratropical zonal wave trains also exert impacts on the East Asian summer climate. In boreal summer, two latitudinally well-separated waveguides are observed over the Eurasian continent (Chowdary et al. 2019). One is the waveguide along the subtropical jet at ~40°N, which is responsible for the circumglobal teleconnection pattern and the Silk Road pattern (Ding and Wang 2005; Hong and Lu 2016). The other is along the large meridional gradient of static stability in northern

Eurasia (Iwao and Takahashi 2008; Xu et al. 2019). The Rossby wave excited by the summer North Atlantic Oscillation (SNAO; Folland et al. 2009; Osborne et al. 2020) tends to propagate along this high-latitude waveguide (Wu et al. 2009; Yamaura and Tomita 2011; Li and Ruan 2018). The zonal wave trains along these two waveguides not only modulate large-scale components of the EASM (e.g., WNPSH and Okhotsk high) but also organize a quasi-stationary trough or ridge in the upper troposphere, bringing anomalous weather in East Asia (Nakamura and Fukamachi 2004; Kosaka et al. 2011; Orsolini et al. 2015; Liu et al. 2019).

All of these studies suggest that East Asian HREs can be determined by both local (i.e., synoptic conditions) and remote processes (i.e., teleconnections). This was also the case for the HREs in South Korea in the summer of 2020 (hereafter, referred to as HREs unless otherwise specified). As shown below, the record-breaking summer rainfall in South Korea was mainly caused by consecutive HREs, but their synoptic natures dramatically varied from one month to another. While the HREs from late June to late July were caused by extratropical cyclones (ETCs), the subsequent HREs were mainly caused by MRB from late July to mid-August. Later, the HREs from late August to early September were triggered by tropical cyclones (TCs). The transition of HRE types from ETC-related ones to MRB-related ones in late July was quite sudden. We suggest that the atmospheric teleconnections induced by the SCS convection and SNAO played a critical role in their rapid transition.

The rest of this paper is organized as follows. Data and methodology are briefly introduced in section 2. Section 3 presents an overview of the 2020 summer rainfall, including HREs. In section 4, synoptic condition of the HREs and subseasonal variation of monsoon circulation are investigated. The role of large-scale circulations is explored in section 5. Further discussion is given in section 6, and the main findings are summarized in section 7.

2. Data and method

The hourly precipitation data recorded at synoptic weather stations of the KMA are used to analyze both the 2020 summer rainfall (91 stations; see Fig. S1 in the online supplemental material for their spatial distribution) and the climatology for the period of 1971–2020 (45 stations). The weather stations on Jeju Island are excluded because of different synoptic variability from those in the Korean Peninsula. To investigate atmospheric circulations, we use the 6-hourly Japanese 55-year Reanalysis (JRA-55; Kobayashi et al. 2015) interpolated onto a 1.25° × 1.25° spatial resolution for the period of 1979–2020. Convective activity in the tropical ocean is quantified by using the daily interpolated outgoing longwave radiation (OLR) at a 2.5° × 2.5° spatial resolution from the National Oceanic and Atmospheric Administration (NOAA; Liebmann and Smith 1996) for the same analysis period. The daily index of boreal summer intraseasonal oscillation (BSISO; Lee et al. 2013), provided by the Asia Pacific Economic Cooperation (APEC) Climate Center (APCC), is also used for the period of 1981–2020. For all variables, the anomaly is defined as a deviation from the long-term climatology at each calendar day.

The HREs in June–September 2020 are identified with the KMA criteria as in Park et al. (2021b). Specifically, an event with 12-h accumulated rainfall greater than 110 mm at any single station is defined as an HRE. Individual HREs are considered to be independent if they are separated for at least 12 h. This allows a total of 15 HREs, as listed in Table 1.

3. Overview of the 2020 summer rainfall

a. Record-breaking summer rainfall

Figure 1a shows the yearly variation of the June–September accumulated rainfall in South Korea. The summer rainfall exhibits substantial interannual variability with more frequent wet summers in the last two decades (see sky-blue bars). In 2020, the summer rainfall amount was 1250 mm, 53% greater than climatology, breaking the record in the past 50 years. This unprecedented rainy summer emerged after 7-yr-long dry summers (see orange bars).

Figure 1b presents the subseasonal variation of the daily rainfall in 2020 (bar) and its long-term climatology (line). Climatologically, there are two rainfall peaks, i.e., one in mid-July and the other in late August. They are well divided by a relatively dry spell in between (Lee et al. 2017). In 2020, however, the first rainfall peak appeared in early August, about 25 days later than the climatological first peak. The withdrawal of the first rainy period was also delayed by about 15 days compared to the climatological withdrawal in late July. In mid-August, rainfall amount sharply decreased. It was then followed by the second rainy period from late August to mid-September.

Figure 1c shows the hourly time series of the maximum 12-h accumulated rainfall amounts across 91 weather stations operated in 2020. As summarized in Table 1, a total of 15 HREs are identified from June to September with ~73% (11 HREs) in 29 June–15 August. As described below, they exhibit distinct synoptic characteristics between the two subperiods: 29 June–27 July (P1; sky-blue shading) and 28 July–15 August (P2; pink shading). The present study focuses on these HREs in P1 and P2.

b. Weather patterns of the HREs

The weather patterns of all HREs are briefly reviewed in this section. Figure 2 presents the geopotential height (GPH) and relative vorticity at 850 hPa for all HREs at the time when the maximum 12-h accumulated rainfall was observed (see Table 1). The relative vorticity is smoothed to a T42 spatial resolution to distinguish synoptic-scale disturbances from mesoscale perturbations. In Fig. 3, the infrared satellite images are shown for all HREs.

Although individual HREs have different background conditions, they can be classified into four synoptic categories: 1) MRB, 2) ETC, 3) extratropical transition (ET), and 4) TC. While the HRE 1 developed along the early MRB (Figs. 2a and 3a), the subsequent HREs 2–5 in P1 were triggered by the ETCs (Figs. 2b–e). The cold or occluded front was well defined in Figs. 3b–e as a key feature of the ETC. Although the HREs 2 and 3 accompanied the zonally organized MRB, the MRB was

TABLE 1. List of the HREs in June–September 2020. MRB, ETC, ET, and TC in the last two columns denote the monsoon rainband, extratropical cyclone, extratropical transition, and tropical cyclone, respectively. HRE ID (third column) follows the temporal order. The TC name is indicated in the rightmost column. See Fig. S2 for the track of each TC.

		HRE					
Period		ID	Date	Max 12-h rainfall	Max 1-h rainfall	Synoptic system	Remark
First rainy period (from early Jun to mid-Aug)		1	1200–2000 UTC 12 Jun	134.3 mm (1900 UTC 12 Jun)	50.1 mm (1500 UTC 12 Jun)	MRB	
	P1	2	1100 UTC 29 Jun–7 UTC 30 Jun	187.0 mm (0000 UTC 30 Jun)	56.3 mm (2300 UTC 29 Jun)	ETC	
		3	1500 UTC 9 Jul–0600 UTC 10 Jul	207.9 mm (0000 UTC 10 Jul)	54.8 mm (0300 UTC 10 Jul)	ETC	
		4	1300 UTC 12 Jul–0200 UTC 13 Jul	151.1 mm (1900 UTC 12 Jul)	31.8 mm (2200 UTC 12 Jul)	ETC	Additional contribution of MRB
		5	0600 UTC 23 Jul–0000 UTC 24 Jul	210.7 mm (1500 UTC 23 Jul)	70.4 mm (1300 UTC 23 Jul)	ETC	
	P2	6	1800 UTC 28 Jul–0400 UTC 30 Jul	191.4 mm (2200 UTC 28 Jul)	55.5 mm (0000 UTC 29 Jul)	MRB	
		7	1300 UTC 1 Aug–1000 UTC 3 Aug	254.8 mm (2100 UTC 1 Aug)	69.8 mm (1400 UTC 2 Aug)	MRB	
		8	2300 UTC 4 Aug–0200 UTC 5 Aug	115.9 (0000 UTC 5 Aug)	26.8 mm (2300 UTC 4 Aug)	MRB	Indirect contribution of Hagupit
		9	1600 UTC 5 Aug–0000 UTC 6 Aug	134.0 mm (2000 UTC 5 Aug)	42.6 mm (2100 UTC 5 Aug)	ET	Hagupit
		10	2200 UTC 6 Aug–0700 UTC 8 Aug	344.4 mm (2300 UTC 7 Aug)	81.5 mm (2200 UTC 7 Aug)	MRB	
		11	2000 UTC 8 Aug–0700 UTC 9 Aug	132.5 mm (2300 UTC 8 Aug)	38.0 mm (2300 UTC 8 Aug)	MRB	
		12	0800 UTC 10 Aug–2000 UTC 10 Aug	118.2 mm (1800 UTC 10 Aug)	38.5 mm (1400 UTC 10 Aug)	MRB	Indirect contribution of Jangmi
Second rainy period (from late Aug to mid-Sep)		13	0400 UTC 26 Aug–1400 UTC 26 Aug	139.9 mm (0900 UTC 26 Aug)	48.2 mm (1200 UTC 26 Aug)	TC	Bavi
		14	0300 UTC 2 Sep–2200 UTC 2 Sep	234.0 mm (1300 UTC 2 Sep)	57.4 mm (0900 UTC 2 Sep)	TC	Maysak
		15	1500 UTC 6 Sep–0600 UTC 7 Sep	224.0 mm (2200 UTC 6 Sep)	55.9 mm (2200 UTC 6 Sep)	TC	Haishen

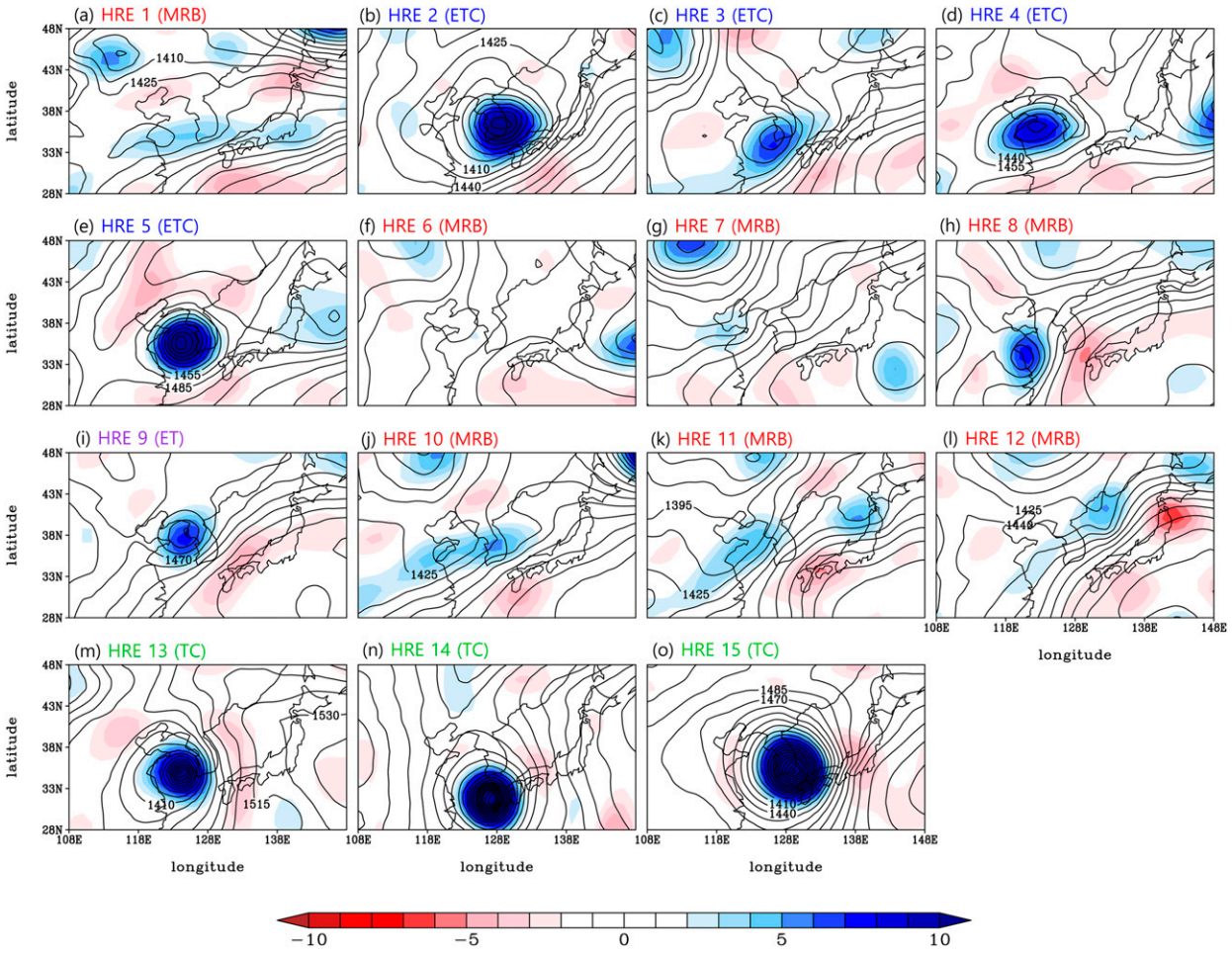

FIG. 2. The 850-hPa GPH (contours, gpm) and relative vorticity (shading, $10^{-5}\,s^{-1}$) truncated at T42 spatial resolution for all HREs listed in Table 1. A snapshot at the time of a maximum 12-h rainfall (adjusted to the nearest 6-hourly mark) is shown. The title of each panel is colored in accordance with the associated synoptic systems (red, blue, purple, and green for MRB, ETC, ET, and TC, respectively).

located in the south of the Korean Peninsula (Figs. 3b,c). During the HRE 4, the MRB reached the southern tip of the Korean Peninsula (Fig. 3d), implying its additional contribution to the HRE.

The HREs 6–12 in P2, however, show no signature of ETCs. They mostly developed along the MRB over the Korean Peninsula (Figs. 2f–l and 3f–l), except for the HRE 9 which was driven by the ET of TC Hagupit (Figs. 2i and 3i). The HREs 8 and 12 were also indirectly influenced by TCs Hagupit and Jangmi, which were located over eastern China and the northeast of the Korean Peninsula, respectively (Figs. 2h,l and 3h,l). In the case of HREs 6–8 and 10–12, cyclonic circulation appeared in northeastern China (Figs. 2f–h,j–l), implying their partial contribution to the formation of the MRB over the Korean Peninsula.

The last three HREs (HREs 13–15) directly resulted from TCs Babi, Maysak, and Haishen, which approached the southwest, south, southeast of the Korean Peninsula, respectively (Figs. 2m–o and 3m–o). The TC tracks involved in these HREs are illustrated in Fig. S2.

Table 1 summarizes the nature of each HRE. It is evident that the HRE type abruptly changed from ETC to MRB in late July and then to TC in late August (see also Fig. 1c). Although the TCs and their contribution to the late-EASM rainfall are reasonably well understood (e.g., Guo et al. 2017), the rapid transition from ETC-related HREs to MRB-related HREs is not well documented. Such a transition is rare, and not observed in China and Japan in the summer of 2020. Note that most HREs in China and Japan occurred by the enhanced MRB (Liu et al. 2020; Takaya et al. 2020; Araki et al. 2021; Horinouchi et al. 2021).

This study mainly addresses the non-TC HREs in P1 and P2, and their transition. Note that the HREs occurred intermittently in P1, whereas those in P2 occurred somewhat persistently (Fig. 1c). Spatially, the HREs in P1 were concentrated along the southern and eastern coasts of the Korean Peninsula (Fig. S1a). In P2, the western half of the country, which is the upwind side of north–south-elongated mountain ranges, was more affected by the HREs (Fig. S1b).

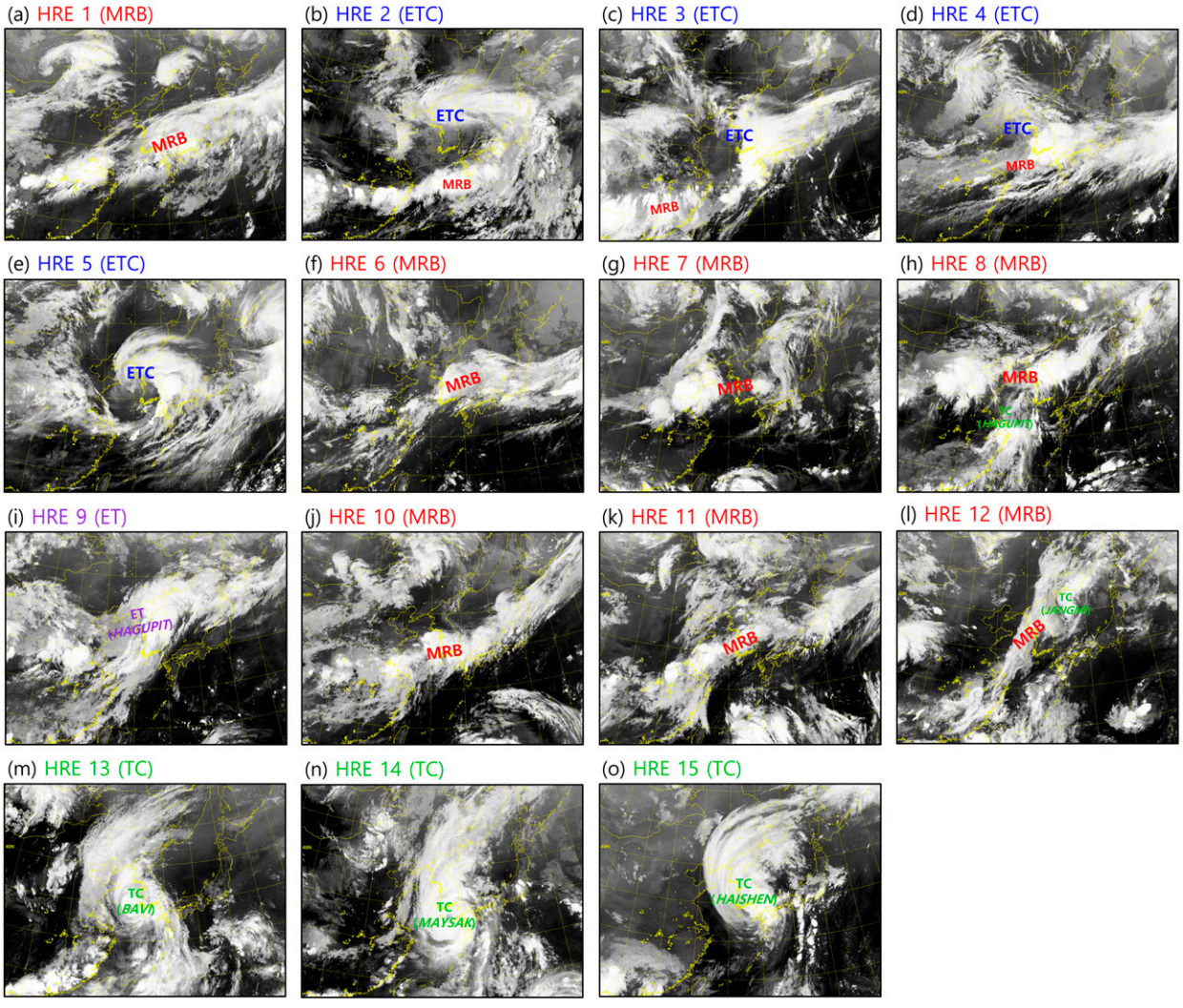

FIG. 3. As in Fig. 2, but for satellite images (10.5-μm infrared channel) obtained from *Geostationary Korea Multi-Purpose Satellite-2A*.

These spatiotemporal differences are closely related with HRE-type differences.

4. Subseasonal variation of the HREs and background flow

a. Synoptic characteristics of the HREs in P1 and P2

Composite map shows that the synoptic pattern of the HREs in P1 is characterized by the ETC in the southwest of the Korean Peninsula (Fig. 4a). This cyclone accompanies a large amount of moisture transport on its southeastern flank (see vectors). Here the moisture transport is quantified by integrating water vapor transport from 1000 to 300 hPa:

$$\mathrm{IVT} = |\mathbf{IVT}|, \quad \text{with}$$

$$\mathbf{IVT} = \left(-\frac{1}{g}\int_{1000\mathrm{hPa}}^{300\mathrm{hPa}} uq\,dp\right)\mathbf{x} + \left(-\frac{1}{g}\int_{1000\mathrm{hPa}}^{300\mathrm{hPa}} vq\,dp\right)\mathbf{y},$$

where g is the gravitational acceleration; u and v are the zonal and meridional winds, respectively; q is the specific humidity; p is the atmospheric pressure; and $\mathbf{x}$ and $\mathbf{y}$ are the unit vectors in the zonal and meridional directions, respectively. In Fig. 4c, the warm sector of the ETC is manifested by high 850-hPa equivalent potential temperature (θ_e). Likewise, low θ_e appears on the rear side of the ETC where a dry conveyor belt intrudes (Browning 1990). Such moisture distributions are also evident in the satellite images (see Figs. 3b–e).

Figure 4b shows that a strong upward motion at 500 hPa is located on the east of the upper-level PV intrusion (black contours) and south of the upper-level jet entrance (shading), a favorable condition for a dynamic ascent (Park et al. 2021b). The meandering upper-level PV further indicates the baroclinic nature of the ETC. When the ETC develops, the WNPSH whose boundary is often identified by the 5840- and 5880-gpm lines at 500 hPa (e.g., Seo et al. 2011; Ren et al. 2015) is positioned south of Japan (see thick contours in Fig. 4c).

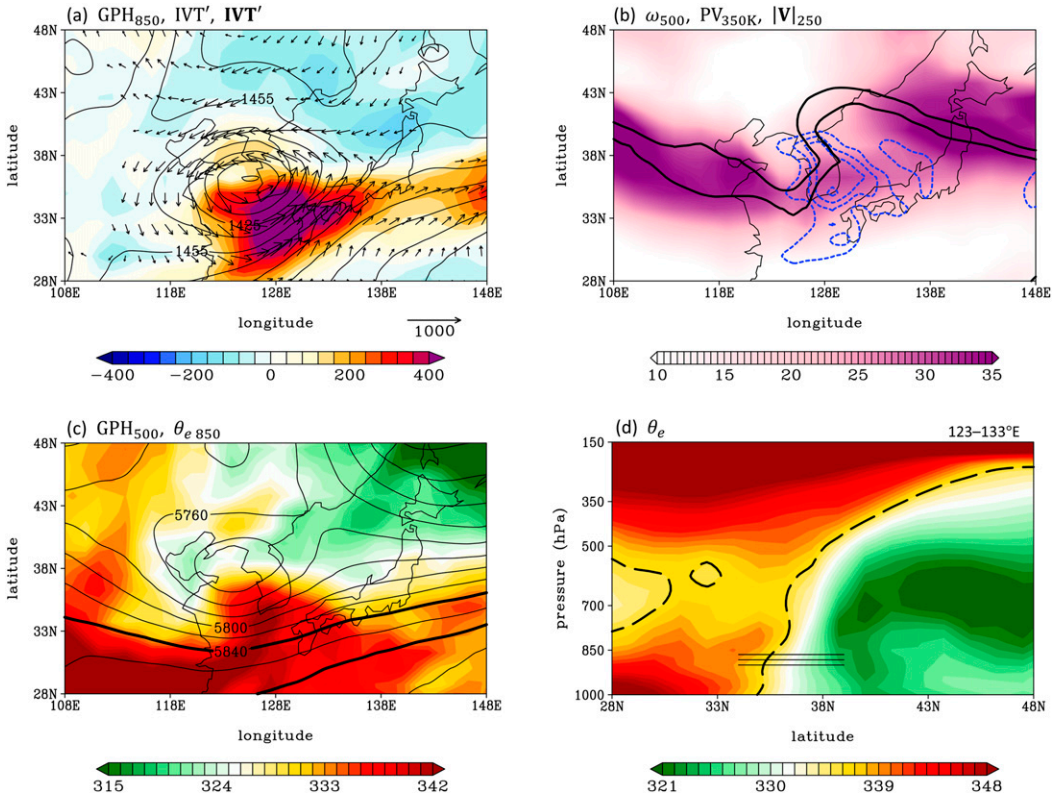

FIG. 4. Composited synoptic structures of the four HREs in P1 (HREs 2–5 in Table 1). (a) GPH (contours, gpm) at 850 hPa, IVT anomaly (shading, kg m^{-1} s^{-1}), and **IVT** anomaly (vectors, >100 kg m^{-1} s^{-1}). (b) Vertical motion at 500 hPa (blue contours with a 0.2-Pa s^{-1} interval), 1.5- and 3-PVU (1 PVU = 10^{-6} K kg^{-1} m^2 s^{-1}) PV at the 350-K isentropic surface (black contours), and horizontal wind speed at 250 hPa (shading, m s^{-1}). (c) GPH at 500 hPa (contours, gpm) and θ_e at 850 hPa (shading, K). The 5840- and 5880-gpm contours are highlighted with thick lines. (d) Latitude–pressure cross section of θ_e (shading, K) averaged over 123°–133°E. The 336-K θ_e is highlighted with a dashed line. The approximate meridional location of South Korea is denoted with three horizontal black lines.

Figure 4d shows the vertical cross section of θ_e. A large meridional gradient is evident across the Korean Peninsula with a poleward tilt, implying a strong baroclinicity. However, its vertical gradient is rather small. This implies that the HREs in P1 occurred under moist-adiabatically near-neutral or only weakly unstable condition.

In P2, the HREs show different dynamical and thermodynamical features from those in P1. Here, the HRE 9 is excluded because it was driven by an ET, unlike the other HREs in P2. Around the Korean Peninsula, no ETC appears (Fig. 5a). Instead, a large amount of moisture is transported toward the Korean Peninsula along the WNPSH boundary. This is a typical circulation pattern favorable for the enhanced MRB (Ninomiya and Shibagaki 2007). The continental low, which is observed in northeastern China (see 1425-gpm contour), likely in part contributes to the formation of a confluent zone over the Korean Peninsula by blocking the northward expansion of the WNPSH. Figure 5b shows that the upper-level jet (shading) and high PV (black contours) are positioned more northward but less undulating than those in P1. The midlevel upward motion (blue contours) is somewhat elongated to the south of the upper-level high PV. This result is consistent with Horinouchi (2014) and Horinouchi and Hayashi (2017), who asserted that given the southwesterly low-level moisture transport, the precipitation band can be enhanced on the southern side of the upper-level high PV although it is only weakly undulating. The upward motion in P2 is notably weaker than that in P1 despite similar or stronger rainfall intensity (see Figs. 1c).

The weak synoptic conditions (e.g., absence of ETC, zonally elongated upper-level PV and weak gridscale vertical motion) imply that the HREs in P2 mainly resulted from local instability within the MRB. The moist-adiabatically unstable condition, as inferred from $\partial\theta_e/\partial z < 0$ in the lower troposphere (Fig. 5d), supports this conjecture. The 5840- and 5880-gpm lines of the 500-hPa GPH are located directly over the Korean Peninsula (Fig. 5c), where a strong positive IVT anomaly is observed (see Fig. 5a).

By comparing Figs. 4 and 5, the HREs in P1 and those in P2 are clearly differentiated by their synoptic features. For the HREs in P1, the circulation pattern shows the feature of baroclinically developing ETCs. In contrast, the HREs in P2 is characterized by the strong southwesterly moisture

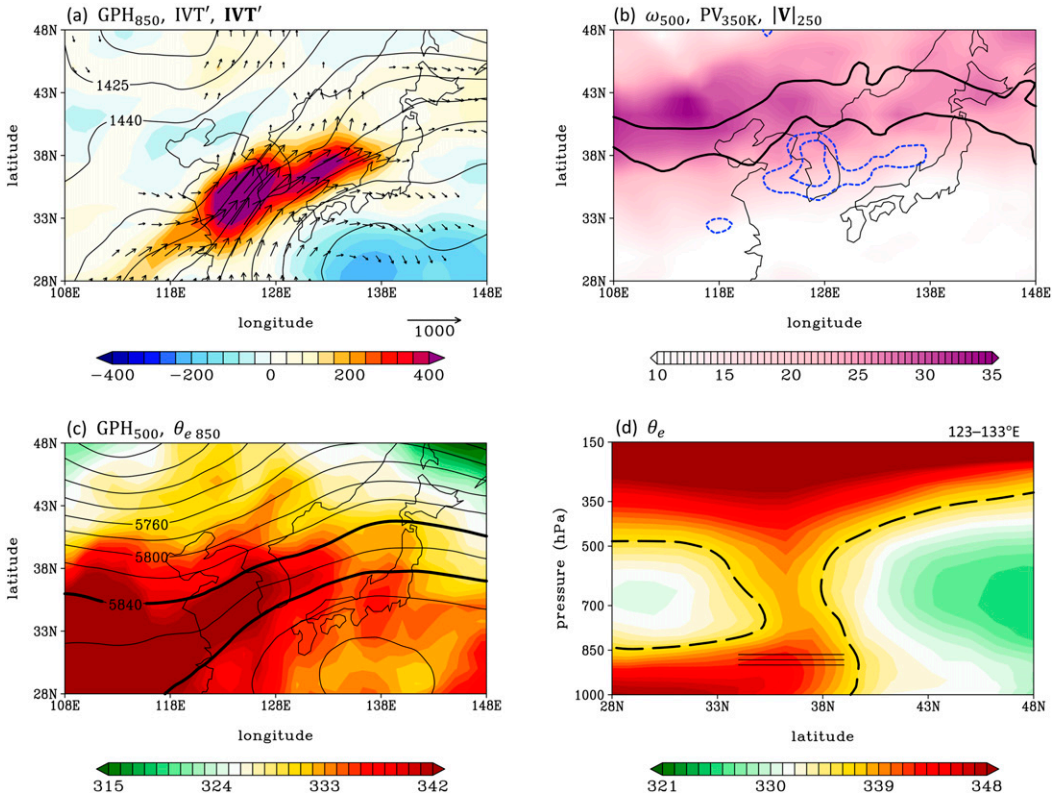

FIG. 5. As in Fig. 4, but for the six HREs in P2 (HREs 6–8 and HREs 10–12 in Table 1).

transport along the northern edge of the WNPSH without developing ETC.

b. *Background flows in P1 and P2*

Consistent with HRE changes, EASM circulation abruptly changed from P1 to P2. Figure 6 presents the time–latitude evolution of the IVT anomaly and latitudinal position of the WNPSH boundary averaged over 123°–133°E. To smooth out the short-term fluctuation, a 9-day moving average is applied. In P1, the 5840-gpm line was located south of its climatological position (cf. thick black and green lines). As a result, the monsoonal IVT anomalously intensified at approximately 30°N but weakened in the north, including South Korea. Note that the positive IVT anomaly over South Korea in Fig. 4a is a result of transient moisture supply by the ETC, not by the quasi-stationary monsoon flow along the WNPSH boundary. In late July, however, the 5840-gpm line abruptly shifted northward. The 5880-gpm line, whose climatology is not identified anymore, also shifted northward, forming an enhanced pressure gradient along the WNPSH boundary. This allowed

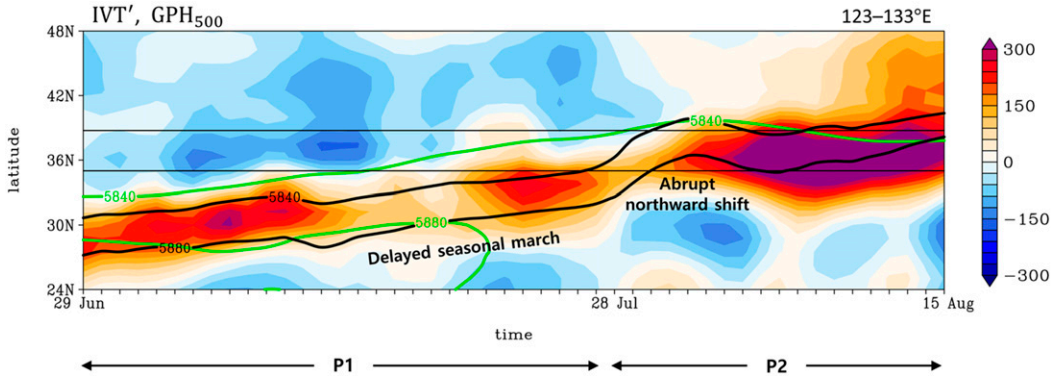

FIG. 6. Latitude–time evolution of the IVT anomaly (shading, kg m^{-1} s^{-1}), 5840- and 5880-gpm GPHs at 500 hPa (thick black line) and their climatologies (thick green line) averaged over 123°–133°E during the period of 29 Jun–15 Aug 2020 (P1 + P2). A 9-day moving average is applied. The approximate meridional location of South Korea is indicated by two thin black lines.

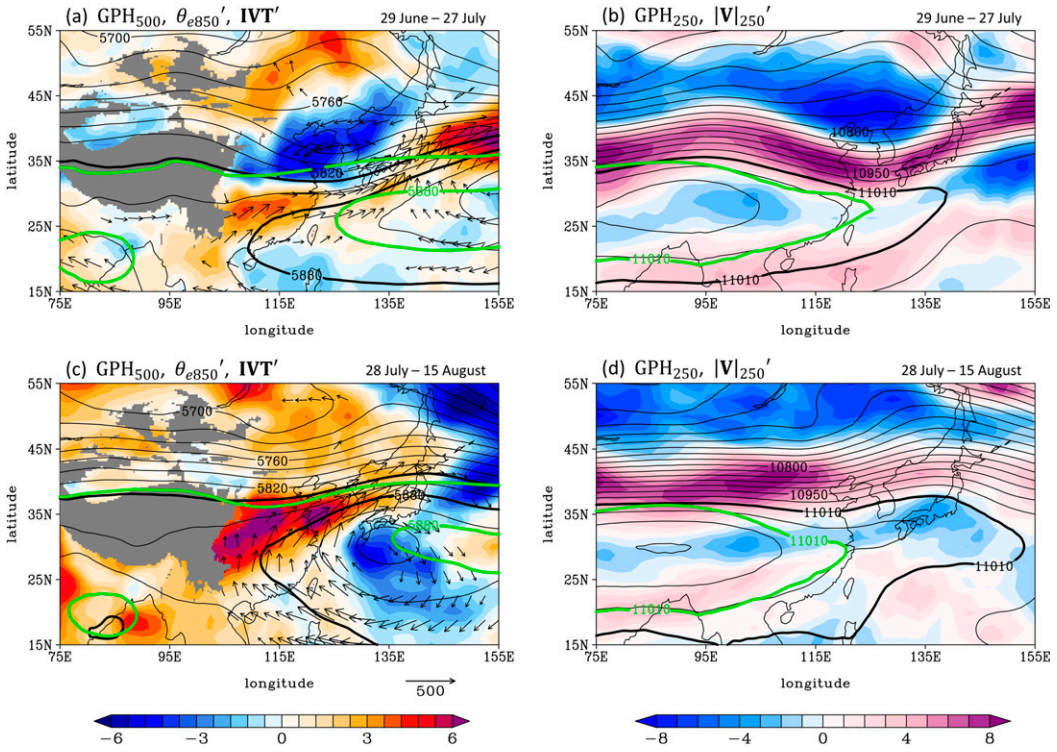

FIG. 7. (a),(c) The GPH at 500 hPa (black contours, gpm), θ_e anomaly at 850 hPa (shading, K), and **IVT** anomaly (vectors, >100 kg m^{-1} s^{-1}) in (a) P1 and (c) P2. The 5840 and 5880 gpm and their climatologies are denoted by thick black and green lines, respectively. The terrain higher than 1500 m is masked by gray shading. (b),(d) The GPH (black contours, gpm) and wind speed anomaly (shading, m s^{-1}) at 250 hPa in (b) P1 and (d) P2. The 11 010-gpm and its climatology are denoted by thick black and green lines, respectively.

anomalously intensified IVT over the latitude of South Korea throughout P2.

To more thoroughly compare the background flows in P1 and P2, the mid and upper-level circulation patterns are examined in Fig. 7 over a broader domain. In P1, the WNPSH largely extends westward (Fig. 7a), as indicated by the 5880-gpm line of the 500-hPa GPH, whose westernmost tip is positioned approximately 15° west of its climatology (cf. thick black and green lines). However, in the north, quasi-stationary ridge and trough are anchored over northeastern China and South Korea, respectively. This persistent trough over South Korea likely blocked the northward march of the WNPSH (cf. 5840-gpm GPH and its climatology between 115° and 135°E), resulting in the southwesterly **IVT** anomaly and positive 850-hPa θ_e anomaly from southeastern China to western Japan. Over South Korea, in contrast, the northeasterly **IVT** anomaly and negative 850-hPa θ_e anomaly are evident.

The upper-tropospheric circulation in P1 is characterized by a large South Asian high (Fig. 7b). Compared to the climatology, the South Asian high extends well eastward to the south of the Korean Peninsula (cf. thick green and black lines). This is consistent with Ren et al. (2015), who found that the westward extension of the WNPSH can be concurrent with the eastward extension of the South Asian high. Along the northern rim of the South Asian high, the upper-level jet is strengthened (shading).

The monsoon circulation depicted in Figs. 7a and 7b is favorable for the MRB to develop from southeastern China to western Japan but not over the Korean Peninsula (see **IVT** anomaly in Fig. 7a). Instead, South Korea was frequently affected by ETCs in P1 (Fig. S3). By analyzing daily weather maps, it turns out that these ETCs were originated from southeastern China, a famous cyclogenesis region (Lee et al. 2020; Kang et al. 2020). Kang et al. (2020) explained that intensification of these ETCs is strongly tied to diabatic processes. Anomalously warm and humid conditions in southeastern China, manifested by a positive 850-hPa θ_e anomaly in Fig. 7a, indeed support the genesis and early development of the ETC in the region (Cho et al. 2018). The intensified upper-level jet on the northern flank of the South Asian high (Fig. 7b) further helps to steer the ETC toward South Korea. The quasi-stationary trough over South Korea (Figs. 7a,b) can also contribute to the deepening of the ETC when it arrives. This can explain why four HREs occurred in P1, although the MRB was southward from the Korean Peninsula.

The monsoon circulation in P2 is very different from that in P1. The most important feature is the northward expansion of the WNPSH (Fig. 7c), which is also evident in Fig. 6. As the quasi-stationary trough, which is observed over South Korea in P1, disappears in P2, the 5840- and 5880-gpm lines jump northward. Although this can be partly due to

the seasonal march of EASM, the abrupt expansion of the WNPSH is well distinguished from its climatological evolution. Note that the 5880-gpm line, whose climatology is confined to the southeast of Japan, locates immediately south of the 5840-gpm line (see also Fig. 6). This means the enhanced pressure gradient along the northern boundary of the WNPSH, creating the strong southwesterly **IVT** anomaly toward Korea. Consistently, the positive 850-hPa θ_e anomaly is widely distributed from the leeward side of the Tibetan Plateau to the Korean Peninsula. This strong quasi-stationary moisture transport along the WNPSH boundary likely allowed MRB to develop over the Korean Peninsula.

In the upper troposphere, the South Asian high farther extended eastward (Fig. 7d). Consistent with the northward expansion of the WNPSH, the eastern ridge of the South Asian high shifted northward (see thick black line). The upper-level jet is also intensified in the north of South Korea, which provides a favorable condition for the precipitation band over the Korean Peninsula. As the overall monsoon system moved northward, the ETC tracks also jumped to higher latitudes, no longer passing over South Korea (Fig. S3).

5. Possible mechanisms of the monsoon circulation change from P1 to P2

The monsoon circulation during P1 is exceptional in that the WNPSH anomalously extended westward, but its northward march was delayed. However, the WNPSH suddenly expanded northward in late July, transporting a large amount of moisture toward the Korean Peninsula during P2. This section suggests the possible mechanisms for this abrupt change in monsoon circulation (Figs. 6 and 7), which is greatly responsible for the distinct synoptic features of the HREs between P1 and P2 (Figs. 4 and 5).

a. Meridional wave train by the SCS convection

Figures 8a and 8b present the 500-hPa streamfunction (ψ), OLR and 500-hPa wind anomalies averaged over P1 and P2, respectively. In P1, positive OLR and ψ anomalies appear over the SCS (Fig. 8a). These suppressed convection and anticyclonic circulation anomalies, which are consistent with the westward extension of the WNPSH (see Fig. 7a), can act as a source of stationary Rossby wave. The resulting wave train forms tripole ψ anomalies in the meridional direction, i.e., anticyclonic anomaly over the SCS, cyclonic anomaly over the Korean Peninsula and anticyclonic anomaly over northeastern China. This is reminiscent of the PJ pattern (Nitta 1987; Kosaka and Nakamura 2006), although the wave train pattern is slightly different from a canonical PJ pattern (see section 5c for details). The associated wave activity flux defined by Takaya and Nakamura (2001) is dominant in the lower troposphere (Fig. S4a), which is a typical feature of the PJ pattern (Kosaka and Nakamura 2006).

It is important to note from Fig. 7a that the cyclonic lobe of the wave train is consistent with the quasi-stationary trough over South Korea. This implies that the delayed northward march of the WNPSH in P1 likely resulted from the PJ-like pattern forced by the suppressed SCS convection. The anticyclonic lobe over northeastern China is also consistent with the

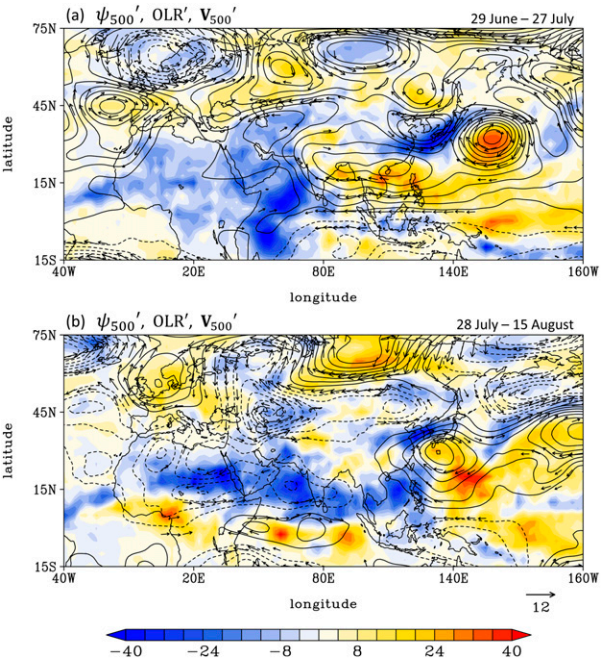

FIG. 8. The ψ anomaly at 500 hPa (contours with a 0.1×10^{-7} m^2 s^{-1}), horizontal wind anomaly at 500 hPa (vectors, >3 m s^{-1}), and OLR anomaly (shading, W m^{-2}) in (a) P1 and (b) P2.

quasi-stationary ridge in Fig. 7a. The prolonged MRB to the south of the Korean Peninsula is manifested by a negative OLR anomaly from southeastern China to western Japan. To the east of Japan, an anticyclonic anomaly is also observed, which is likely a wave response to the enhanced convection of the prolonged MRB.

In P2, the OLR anomaly over the SCS switches its sign to negative (enhanced convection; Fig. 8b). This leads to the disappearance of the anticyclonic ψ anomaly over the SCS. The anticyclonic anomaly instead becomes dominant in the north, with a center at the right south of western Japan. This anticyclonic anomaly is consistent with the northward expansion of the WNPSH and the enhanced pressure gradient along its northern boundary (see Fig. 7c). The line-shaped negative OLR anomaly on the northern rim of the anticyclonic anomaly manifests the enhanced MRB over the Korean Peninsula. The anticyclonic ψ anomaly over northeastern China, which is maintained in P1, also changes to a cyclonic ψ anomaly. Although further analyses are required, the disappearance of the anticyclonic anomaly over the SCS and the subsequent northward expansion of the WNPSH are likely circulation response to the enhanced SCS convection. In section 5c, the role of the SCS convection in the EASM circulation anomaly is further evaluated by conducting a long-term data analysis.

b. Zonal wave train by the SNAO

Figure 8 also shows a zonal wave train in high latitudes. In P1, for instance, a wave train starting from the cyclonic ψ anomaly over the eastern North Atlantic develops downstream (Fig. 8a). The wave train pattern contains an anticyclonic lobe over the

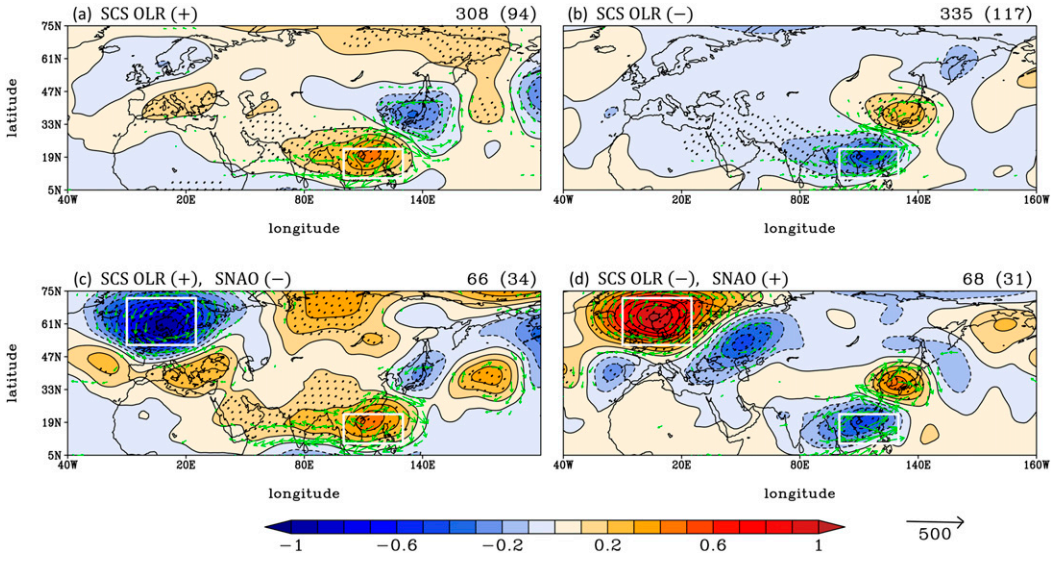

FIG. 9. The 500-hPa ψ anomaly (contours and shading, 10^{-7} m^2 s^{-1}) and **IVT** anomaly (vectors, kg m^{-1} s^{-1}) when the SCS OLR index is (a) above $+1.0\sigma$ and (b) below -1.0σ for the period of 29 Jun–15 Aug from 1979 to 2019. (c),(d) As in (a) and (b), but for (c) the SCS OLR index $> +1.0\sigma$ and the SNAO index $< -1.0\sigma$ and (d) the SCS OLR index $< -1.0\sigma$ and the SNAO index $> +1.0\sigma$. The statistically significant ψ anomalies at the 90% confidence level based on the Student's t test are stippled. Only the statistically significant **IVT** anomalies at the same confidence level are shown. Two boxed regions denote the SCS (10°–22.5°N, 100°–130°E) and eastern North Atlantic (52°–72°N, 10°W–25°E). The number of days considered is indicated in the top-right corner of each plot. The number of degrees of freedom, by considering consecutive days as one event, is given in parentheses.

Ural Mountains, a cyclonic lobe over central Siberia, and an anticyclonic lobe over northeastern China. This pattern, which has an equivalent barotropic structure with a stronger wave activity in the upper troposphere (Fig. S4a), resembles the typical teleconnection pattern over northern Eurasia in the boreal summer (Iwao and Takahashi 2008; Xu et al. 2019). The circulation anomaly over the North Atlantic, which is similar to the negative phase of the SNAO, suggests that the SNAO-related divergent flow might be a source of high-latitude wave train (Wu et al. 2009; Li and Ruan 2018).

In P2, the ψ anomaly over the eastern North Atlantic changes its sign to positive (Fig. 8b), exhibiting a positive SNAO. Note that the northern Eurasian wave pattern also shows opposite sign to that in P1. This implies that the abrupt change in monsoon circulation from P1 to P2 was also likely influenced by the SNAO-induced zonal wave train. Recently, Liu et al. (2020) proposed the subseasonal phase transition of the SNAO as a key regulator of extreme rainfall around the Yangtze River in the early summer of 2020. They suggested that a positive SNAO on 11–25 June and a negative SNAO on 30 June–13 July led to the different synoptic characteristics of quasi-stationary monsoon front between the two periods. However, their analysis cannot be directly applied to the present study because of different analysis period. The possible role of the SNAO in the East Asian circulation anomalies in P1 and P2 is further explored in section 5c.

c. *Combined effect of the SCS convection and SNAO*

To evaluate the general role of the SCS convection and SNAO on EASM circulation, composite maps are constructed for the days when SCS OLR anomaly is well defined or when both SCS OLR and SNAO anomalies are at work for the period of 29 June–15 August from 1979 to 2019 (Fig. 9). Note that the year 2020 is excluded. Here, the SCS convection is indexed as the area-mean OLR anomaly over the SCS (10°–22.5°N, 100°–130°E). In a similar way, the SNAO index is defined as the area-mean 500-hPa GPH anomaly over the eastern North Atlantic (52°–72°N, 10°W–25°E). Only the days when each index is greater than ± 1.0 standard deviation (σ) in magnitude are selected to increase the signal-to-noise ratio. The statistically significant values at the 90% confidence level are determined based on the Student's t test. When counting the number of degrees of freedom, continuous days with no break are considered as a single event.

The composite 500-hPa ψ anomaly for the SCS OLR index above 1.0σ (i.e., enhanced SCS convection) exhibits a canonical PJ pattern (Fig. 9a). An opposite phase of the PJ pattern is also obtained for the SCS OLR index below -1.0σ (i.e., suppressed SCS convection; Fig. 9b). These wave patterns along the east coast of the Eurasian continent are somewhat different from those in the summer of 2020. For the suppressed SCS convection, the cyclonic lobe centered to the east of the Korean Peninsula is excessively extended in a northwestward-southeastward direction (Fig. 9a), while the lobe in P1 is more localized over the Korean Peninsula (Fig. 8a). The anticyclonic ψ anomaly over northeastern China, which is evident in P1, also does not appear in Fig. 9a. Similarly, the anticyclonic lobe for the enhanced SCS convection is excessively extended in a northwestward-southeastward

direction (Fig. 9b). It contrasts with the case in P2, which is characterized by the northern boundary of the anticyclonic anomaly right over the Korean Peninsula (Fig. 8b). These results indicate that the SCS convection alone may not fully explain the anomalous background flow and its abrupt change from P1 to P2.

When both the SCS convection and SNAO are considered, the East Asian circulation anomalies more resemble those in the summer of 2020. With the SCS OLR index above 1.0σ and the SNAO index below -1.0σ (Fig. 9c), tripole ψ anomalies are organized over the SCS, east of the Korean Peninsula and northeastern China. Although the cyclonic lobe is slightly shifted eastward compared to that in P1, it is well sandwiched between the two anticyclonic lobes in the north and south as in P1 (Fig. 8a). An anticyclonic anomaly to the east of Japan is also better captured.

The composited ψ anomalies for the SCS OLR index below -1.0σ and the SNAO index above 1.0σ also depict a qualitatively more similar pattern to the case of P2 (Fig. 9d). Compared to Fig. 9b, the spatial extent of the anticyclonic lobe is noticeably reduced due to the cyclonic ψ anomaly in the north. The horizontal gradient of the anticyclonic ψ anomaly is also stronger over the Korean Peninsula. This allows a stronger southwesterly **IVT** anomaly toward the Korean Peninsula (cf. vectors in Figs. 9b,d), providing a favorable condition for MRB development. However, the cyclonic anomaly over the SCS in Fig. 9d does not match with no anomaly in Fig. 8b. This may suggest that additional factors may play a role in setting low-latitude circulation in P2. Although not shown, the overall result is not sensitive to the presence or absence of the summertime El Niño–Southern Oscillation signal.

The above results suggest that the anomalous monsoon circulation around the Korean Peninsula and its sharp change from P1 to P2 are likely explained by the combined effects of the SCS convection and SNAO. Figure 10 indeed shows that both the SCS OLR and SNAO indices simultaneously changed their signs at the end of July, although the reason remains to be determined. The previous study by Seo et al. (2012), who attributed the extraordinary behavior of the WNPSH in July 2011 to the joint effect of the SCS convection and SNAO, further strengthens our argument.

It is also worth mentioning that the SNAO index is weakly correlated with the SCS OLR index on interannual time scale ($r = -0.3$, p value $= 0.06$). When their covariability is linearly removed by computing partial correlations, it becomes clearer that the EASM circulation anomalies are significantly affected by the SCS convection with a rather minor contribution of the SNAO (not shown). This is consistent with the composite analysis shown in Fig. 9.

6. Discussion

a. Indo–western Pacific Ocean capacitor (IPOC) effect

The westward extension of the WNPSH and the suppressed convection over the SCS in P1 (see Fig. 7a) are likely the response to a large-scale atmosphere–ocean coupled mode. More specifically, it is speculated that the Indo–western Pacific Ocean capacitor (IPOC) effect (Xie et al. 2009, 2016) has likely played a critical role.

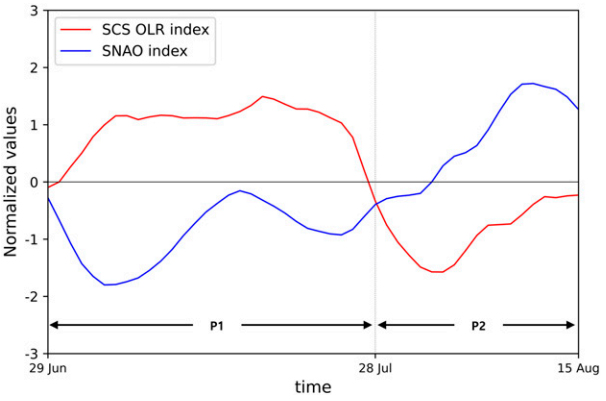

FIG. 10. Daily time series of the SCS OLR index and SNAO index normalized by their one standard deviation during the period of 29 Jun–15 Aug 2020 (P1 + P2). A 9-day running average is applied.

The IPOC effect is briefly summarized as follows. The wintertime El Niño typically decays in the following spring (Tziperman et al. 1998; Kim and An 2021). However, the associated tropical Indian Ocean warming, which is dictated by ocean dynamics and local air–sea interactions (Xie et al. 2002; Du et al. 2009), often persists until early summer, resulting in enhanced convection over the tropical Indian Ocean. This enhanced convection drives eastward-propagating baroclinic Kelvin waves into the equatorial western Pacific as a Gill-type response (Gill 1980). In the lower troposphere, the Kelvin wave–induced Ekman divergence over the subtropical western North Pacific can enhance the anticyclonic circulation.

A similar condition is evident in P1. The 2019/20 wintertime El Niño rapidly decayed in the spring of 2020 (Fig. S5), but the associated sea surface temperature (SST) anomaly of the tropical Indian Ocean remained positive in P1 (Fig. S6). Figure 11a clearly shows the enhanced convection over the tropical Indian Ocean (blue shading) and the divergent near-surface northeasterly anomaly from the SCS to the Bay of Bengal (vectors). This greatly resembles the typical IPOC mode (see Fig. 15 in Xie et al. 2016). Note that the near-surface divergence matches well with the westward extension of the WNPSH in P1 (cf. thick black and green lines).

Takaya et al. (2020) and Zhou et al. (2021) recently indicated that the preceding winter El Niño was not sufficiently strong to allow the IPOC mode. According to their analyses, the tropical Indian Ocean warming in the early summer of 2020 was likely caused not only by the preceding El Niño but also by the super Indian Ocean dipole in August–October 2019. Zhang et al. (2021) further indicated that the exceptionally persistent Madden–Julian oscillation also contributed to the enhanced convection over the Indian Ocean.

The IPOC-driven westward enhancement of the WNPSH was also observed in June, prior to the PJ-like pattern in P1 (Fig. S7). This implies that the suppressed SCS convection in P1, which acts as a source of the PJ-like pattern, likely resulted from the westward extension of the WNPSH forced by the

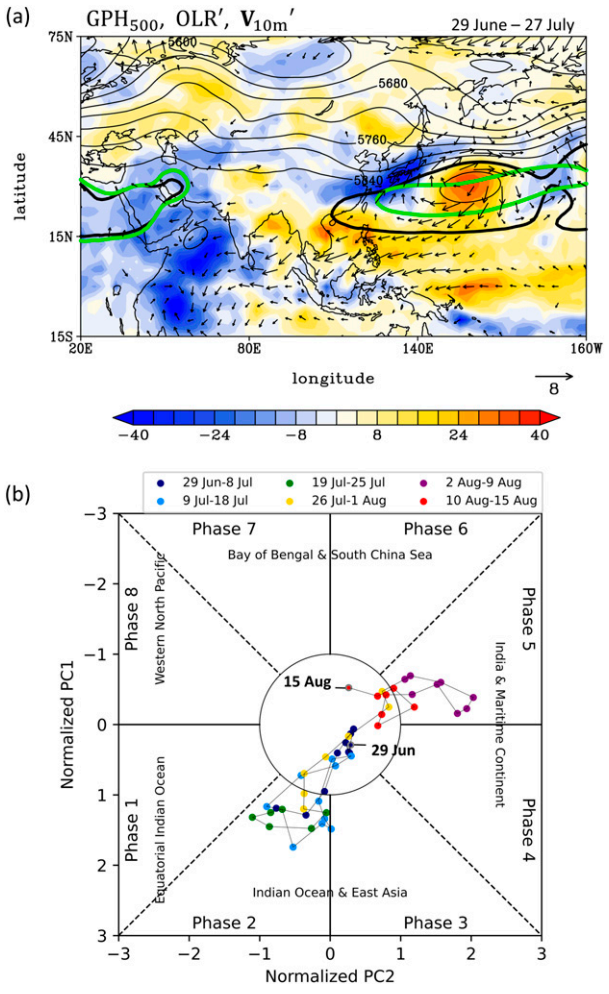

FIG. 11. (a) As in Fig. 8, but for GPH at 500 hPa (black contours, gpm), OLR anomaly (shading, W m^{-2}), and 10-m horizontal wind anomaly (vectors; >1 m s^{-1}) in P1. The 5880 gpm and its climatology are also plotted by thick black and green lines, respectively. (b) Phase diagram of BSISO1 during the period of 29 Jun–15 Aug 2020 (P1 + P2).

IPOC effect. This IPOC–PJ relationship was previously proposed by Xie et al. (2009, 2016) and further supported by a significant correlation between the PJ pattern and the preceding winter El Niño (Kosaka et al. 2011; Kubota et al. 2016). Kim and Kug (2021) recently verified the delayed PJ response to the warm tropical Indian Ocean. They showed that the warm tropical Indian Ocean often induces an anticyclonic anomaly over the subtropical western North Pacific via equatorial Kelvin wave propagation, and the delayed PJ response brings a cold temperature anomaly to the Korea–Japan region.

b. *BSISO*

It is unclear why the OLR anomaly over the SCS sharply changed its sign in late July. Since the SST anomaly over the SCS did not change much from P1 to P2 (Fig. S6), this transition is likely explained by the atmospheric internal variability such as BSISO mode 1 (BSISO1). The BSISO1 phase indeed abruptly changed from P1 to P2 (Fig. 11b). While the BSISO1 was mostly in phase 2 during P1, that during P2 was predominantly in phase 5. Their transition was quite sudden with only a few days of no active BSISO1 in between. Note that the OLR anomalies over the Indo–western Pacific Ocean in P1 and P2 greatly resemble the typical OLR patterns of BSISO1 phases 2 and 5, respectively (cf. Figs. 8 and S8).

c. *Other possible factors*

There might be other factors that affected the record-breaking summer rainfall in South Korea. For example, the westward extension of the WNPSH in P1 may be influenced by the nonlinear interactions between El Niño–Southern Oscillation and the annual cycle of background flow, so-called the combination mode (Stuecker et al. 2013, 2015). According to Stuecker et al. (2015), the combination mode can lead to anomalous anticyclonic circulation over the Northwest Pacific when the La Niña phase grows in the boreal summer, as in June–July 2020 (Fig. S5). This may have constructively worked together with the IPOC effect to enhance the WNPSH in P1.

The upper-level GPH at ~35°–40°N in P1 (Fig. 7b) is reminiscent of the Silk Road pattern (Hong and Lu 2016), which was pointed out by Horinouchi et al. (2021) as a cause of the prolonged heavy rainfall in western Japan in early July 2020. In 2020 summer, the Arctic experienced the amplified warming (Fig. S9a), and the SST in the Northern Hemisphere was anomalously warm almost everywhere except for the equatorial eastern Pacific due to the developing La Niña (Fig. S9b). Their possible impacts on the record-breaking rainfall deserve further attention.

It is notable that the wet summers in Korea have become more frequent in the last two decades compared to the 1970s and 1980s (see blue bars in Fig. 1a). This long-term change may result from the monsoon circulation change in response to anthropogenic warming. By examining regional climate model simulations, Kim et al. (2018) asserted that the intensity and frequency of the Korean HREs will continue to increase in the future. Although the role of anthropogenic warming on the regional HRE is beyond the scope of this study, such analysis (e.g., Imada et al. 2020) would be valuable for better understanding the record-breaking rainfall in 2020 summer.

7. Summary and conclusions

In the summer of 2020, record-breaking monsoon rainfall occurred in South Korea, causing destructive floods across the country. This hydrological extreme was mainly caused by 15 consecutive HREs. These HREs show three distinct synoptic features. All HREs from 29 June to 27 July (P1) were intermittently produced by developing ETCs, whereas those from 28 July to 15 August (P2) persistently occurred along the MRB. The transition from P1 to P2 was quite sudden. This rapid transition of HRE types is distinguished from Chinese and Japanese HREs in June–July 2020, which were mostly dominated by the MRB. After a short dry spell, HREs occurred again in late summer. They are all caused by TCs.

The differing characteristics of the HREs between P1 and P2 are examined in the context of synoptic structures and background monsoon flows. In P1, the WNPSH anomalously extended westward via the IPOC effect. However, its northward expansion was delayed due to a quasi-stationary trough anchored over South Korea. Under this condition, the MRB was maintained to the south of the Korean Peninsula. Instead, the ETCs initiated over southeastern China frequently traveled across the Korean Peninsula, resulting in four HREs. In P2, the WNPSH rapidly expanded northward, and the pressure gradient along its northern boundary was considerably enhanced compared to its climatological state. This allowed strong southwesterly moisture transport toward the Korean Peninsula, forming the MRB over the region. Local convective instability along the MRB triggered six HREs.

The changes in the background flow, which determined synoptic characteristics of the HREs, likely resulted from the combined effect of the SCS convection- and SNAO-related teleconnections. In P1, the convection over the SCS was anomalously suppressed, resulting in a PJ-like pattern. The associated quasi-stationary trough over South Korea hindered the WNPSH from progressing northward. However, the SCS convection became strong in late July. The circulation response to the enhanced convection resulted in an abrupt northward expansion of the WNPSH in P2. Although further analysis is required, the SCS convection change is closely related to the phase change of BSISO1.

On top of the meridional wave train, the SNAO-induced zonal wave train was also organized at high latitudes from the eastern North Atlantic to northeastern China. This zonal wave train changed sign as the SNAO changed from the negative phase in P1 to the positive phase in P2. Although the reason for this synchronized phase change of SCS convection and SNAO is unclear, the long-term data analysis suggests that when the SNAO is accompanied, the SCS convection-induced meridional wave train pattern more successfully mimics the East Asian circulation anomalies in both P1 and P2.

This study demonstrates that the summertime HREs can change their characteristics on a subseasonal time scale. In particular, their synoptic features can be strongly modulated by remote forcings from both tropics and extratropics. This finding suggests that not only the local processes (i.e., synoptic conditions) but also the remote processes (i.e., teleconnections) need to be taken into account for improved understanding and prediction of the HREs in the EASM region. Beyond observational analyses, a numerical experiment with an atmosphere–ocean coupled model would be helpful to confirm the key findings and arguments of the present study.

Acknowledgments. The constructive comments by two anonymous reviewers are greatly appreciated. This work was funded by Korea Meteorological Administration Research and Development Program ''Enhancement of Convergence Technology of Analysis and Forecast on Severe Weather'' under Grant KMA2018-00121.

Data availability statement. The KMA station precipitation data are available at https://data.kma.go.kr/data/grnd/selectAsosRltmList.do?pgmNo=36. The satellite image (10.5-μm infrared channel) from *Geostationary Korea Multi-Purpose Satellite-2A* of KMA is available at https://nmsc.kma.go.kr/enhome/html/satellite/viewer/selectGk2aSatViewer.do?view=basic. The JRA-55 data can be downloaded from https://jra.kishou.go.jp/JRA-55/index_en.html#mirror. The daily interpolated OLR data are available at https://psl.noaa.gov/data/gridded/data.interp_OLR.html. The daily BSISO index is available at https://www.apcc21.org/ser/moni.do?lang=en#grap1.

REFERENCES

Araki, K., T. Kato, Y. Hirockawa, and W. Hashiko, 2021: Characteristics of atmospheric environments of quasi-stationary convective bands in Kyushu, Japan during the July 2020 heavy rainfall event. *SOLA*, **17**, 8–15, https://doi.org/10.2151/sola.2021-002.

Browning, K. A., 1990: Organization of clouds and precipitation in extratropical cyclones. *Extratropical Cyclones: The Erik Palmén Memorial Volume*, C. W. Newton and E. O. Holopainen, Eds., Amer. Meteor. Soc., 129–153.

Cho, H.-O., S.-W. Son, and D.-S. Park, 2018: Springtime extratropical cyclones in Northeast Asia and their impacts on long-term precipitation trends. *Int. J. Climatol.*, **38**, 4043–4050, https://doi.org/10.1002/joc.5543.

Choi, S.-J., D.-H. Cha, and D.-K. Lee, 2008: Simulation of the 18-day summer heavy rainfall over East Asia using a regional climate model. *J. Geophys. Res.*, **113**, D12101, https://doi.org/10.1029/2007JD009213.

Chowdary, J. S., K. Hu, G. Srinivas, Y. Kosaka, L. Wang, and K. K. Rao, 2019: The Eurasian jet streams as conduits for East Asian monsoon variability. *Curr. Climate Change Rep.*, **5**, 233–244, https://doi.org/10.1007/s40641-019-00134-x.

Ding, Q., and B. Wang, 2005: Circumglobal teleconnection in the Northern Hemisphere summer. *J. Climate*, **18**, 3483–3505, https://doi.org/10.1175/JCLI3473.1.

Du, Y., S.-P. Xie, G. Huang, and K. M. Hu, 2009: Role of air–sea interaction in the long persistence of El Niño–induced north Indian Ocean warming. *J. Climate*, **22**, 2023–2038, https://doi.org/10.1175/2008JCLI2590.1.

Folland, C. K., J. Knight, H. W. Linderholm, D. Fereday, S. Ineson, and J. W. Hurrell, 2009: The summer North Atlantic Oscillation: Past, present, and future. *J. Climate*, **22**, 1082–1103, https://doi.org/10.1175/2008JCLI2459.1.

Gill, A. E., 1980: Some simple solutions for heat-induced tropical circulation. *Quart. J. Roy. Meteor. Soc.*, **106**, 447–462, https://doi.org/10.1002/qj.49710644905.

Guo, L., N. P. Klingaman, P. L. Vidale, A. G. Turner, M. Demory, and A. Cobb, 2017: Contribution of tropical cyclones to atmospheric moisture transport and rainfall over East Asia. *J. Climate*, **30**, 3853–3865, https://doi.org/10.1175/JCLI-D-16-0308.1.

Hamada, A., and Y. N. Takayabu, 2018: Large-scale environmental conditions related to midsummer extreme rainfall events around Japan in the TRMM region. *J. Climate*, **31**, 6933–6945, https://doi.org/10.1175/JCLI-D-17-0632.1.

Hirota, N., Y. N. Takayabu, M. Kato, and S. Arakane, 2016: Roles of an atmospheric river and a cutoff low in the extreme precipitation event in Hiroshima on 19 August 2014. *Mon. Wea. Rev.*, **144**, 1145–1160, https://doi.org/10.1175/MWR-D-15-0299.1.

Hong, X., and R. Lu, 2016: The meridional displacement of the summer Asian jet, Silk Road pattern, and tropical SST

anomalies. *J. Climate*, **29**, 3753–3766, https://doi.org/10.1175/JCLI-D-15-0541.1.

Horinouchi, T., 2014: Influence of upper tropospheric disturbances on the synoptic variability of precipitation and moisture transport over summertime East Asia and the northwestern Pacific. *J. Meteor. Soc. Japan*, **92**, 519–541, https://doi.org/10.2151/jmsj.2014-602.

——, and A. Hayashi, 2017: Meandering subtropical jet and precipitation over summertime East Asia and the northwestern Pacific. *J. Atmos. Sci.*, **74**, 1233–1247, https://doi.org/10.1175/JAS-D-16-0252.1.

——, Y. Kosaka, H. Nakamigawa, H. Nakamura, N. Fujikawa, and Y. N. Takayabu, 2021: Moisture supply, jet, and Silk-Road wave train associated with the prolonged heavy rainfall in Kyushu, Japan in early July 2020. *SOLA*, **17B**, 1–8, https://doi.org/10.2151/sola.2021-019.

Imada, Y., H. Kawase, M. Watanabe, M. Arai, H. Shiogama, and I. Takayabu, 2020: Advanced risk-based event attribution for heavy regional rainfall events. *NPJ Climate Atmos. Sci.*, **3**, 37, https://doi.org/10.1038/s41612-020-00141-y.

Iwao, K., and M. Takahashi, 2008: A precipitation seesaw mode between northeast Asia and Siberia in summer caused by Rossby waves over the Eurasian continent. *J. Climate*, **21**, 2401–2419, https://doi.org/10.1175/2007JCLI1949.1.

Jo, E., C. Park, S.-W. Son, J.-W. Roh, G.-W. Lee, and Y.-H. Lee, 2020: Classification of localized heavy rainfall events in South Korea. *Asia-Pac. J. Atmos. Sci.*, **56**, 77–88, https://doi.org/10.1007/s13143-019-00128-7.

Kamae, Y., W. Mei, S.-P. Xie, M. Naoi, and H. Ueda, 2017: Atmospheric rivers over the northwestern Pacific: Climatology and interannual variability. *J. Climate*, **30**, 5605–5619, https://doi.org/10.1175/JCLI-D-16-0875.1.

Kang, J. M., J. Lee, S.-W. Son, J. Kim, and D. Chen, 2020: The rapid intensification of East Asian cyclones around the Korean Peninsula and their surface impacts. *J. Geophys. Res. Atmos.*, **125**, e2019JD031632, https://doi.org/10.1029/2019JD031632.

Kim, G., and Coauthors, 2018: Future changes in extreme precipitation indices over Korea. *Int. J. Climatol.*, **38**, e862–e874, https://doi.org/10.1002/joc.5414.

Kim, S., and J.-S. Kug, 2021: Delayed impact of Indian Ocean warming on the East Asian surface temperature variation in boreal summer. *J. Climate*, **34**, 3255–3270, https://doi.org/10.1175/JCLI-D-20-0691.1.

Kim, S.-K., and S.-I. An, 2021: Seasonal gap theory for ENSO phase locking. *J. Climate*, **34**, 5621–5634, https://doi.org/10.1175/JCLI-D-20-0495.1.

KMA, 2021: Abnormal Climate Report 2020 (in Korean). KMA, 212 pp., http://www.climate.go.kr/home/bbs/view.php?code=93&bname=abnormal&vcode=6494.

Kobayashi, S., and Coauthors, 2015: The JRA-55 Reanalysis: General specifications and basic characteristics. *J. Meteor. Soc. Japan*, **93**, 5–48, https://doi.org/10.2151/jmsj.2015-001.

Kosaka, Y., and H. Nakamura, 2006: Structure and dynamics of the summertime Pacific–Japan teleconnection pattern. *Quart. J. Roy. Meteor. Soc.*, **132**, 2009–2030, https://doi.org/10.1256/qj.05.204.

——, S.-P. Xie, and H. Nakamura, 2011: Dynamics of interannual variability in summer precipitation over East Asia. *J. Climate*, **24**, 5435–5453, https://doi.org/10.1175/2011JCLI4099.1.

Kubota, H., Y. Kosaka, and S.-P. Xie, 2016: A 117-year long index of the Pacific–Japan pattern with application to interdecadal variability. *Int. J. Climatol.*, **36**, 1575–1589, https://doi.org/10.1002/joc.4441.

Lee, D.-K., J.-G. Park, and J.-W. Kim, 2008: Heavy rainfall events lasting 19 days from July 31 to August 17, 1998, over Korea. *J. Meteor. Soc. Japan*, **86**, 313–333, https://doi.org/10.2151/jmsj.86.313.

Lee, J., S.-W. Son, H.-O. Cho, J. Kim, D.-H. Cha, J. R. Gyakum, and D. Chen, 2020: Extratropical cyclones over East Asia: Climatology, seasonal cycle, and long-term trend. *Climate Dyn.*, **54**, 1131–1144, https://doi.org/10.1007/s00382-019-05048-w.

Lee, J. Y., B. Wang, M. C. Wheeler, X. Fu, D. E. Waliser, and I.-S. Kang, 2013: Real-time multivariate indices for the boreal summer intraseasonal oscillation over the Asian summer monsoon region. *Climate Dyn.*, **40**, 493–509, https://doi.org/10.1007/s00382-012-1544-4.

——, and Coauthors, 2017: The long-term variability of Changma in the East Asian summer monsoon system: A review and revisit. *Asia-Pac. J. Atmos. Sci.*, **53**, 257–272, https://doi.org/10.1007/s13143-017-0032-5.

Li, J., and C. Ruan, 2018: The North Atlantic–Eurasian teleconnection in summer and its effects on Eurasian climates. *Environ. Res. Lett.*, **13**, 024007, https://doi.org/10.1088/1748-9326/aa9d33.

Li, R. C. Y., W. Zhou, and T. Li, 2014: Influences of the Pacific–Japan teleconnection pattern on synoptic-scale variability in the western North Pacific. *J. Climate*, **27**, 140–154, https://doi.org/10.1175/JCLI-D-13-00183.1.

Liebmann, B., and C. A. Smith, 1996: Description of a complete (interpolated) outgoing longwave radiation dataset. *Bull. Amer. Meteor. Soc.*, **77**, 1275–1277.

Liu, B., C. Zhu, J. Su, and S. Ma, 2019: Record-breaking northward shift of the western North Pacific subtropical high in July 2018. *J. Meteor. Soc. Japan*, **97**, 913–925, https://doi.org/10.2151/jmsj.2019-047.

——, Y. Yan, C. Zhu, S. Ma, and J. Li, 2020: Record-breaking Meiyu rainfall around Yangtze River in 2020 regulated by the subseasonal phase transition of North Atlantic Oscillation. *Geophys. Res. Lett.*, **47**, e2020GL090342, https://doi.org/10.1029/2020GL090342.

Nakamura, H., and T. Fukamachi, 2004: Evolution and dynamics of summertime blocking over the Far East and the associated surface Okhotsk high. *Quart. J. Roy. Meteor. Soc.*, **130**, 1213–1233, https://doi.org/10.1256/qj.03.101.

Nie, J., and B. Fan, 2019: Roles of dynamic forcings and diabatic heating in summer extreme precipitation in East China and the southeastern United States. *J. Climate*, **32**, 5815–5831, https://doi.org/10.1175/JCLI-D-19-0188.1.

Ninomiya, K., and Y. Shibagaki, 2007: Multi-scale features of the Meiyu-Baiu front and associated precipitation systems. *J. Meteor. Soc. Japan*, **85B**, 103–122, https://doi.org/10.2151/jmsj.85B.103.

Nitta, T., 1987: Convective activities in the tropical western Pacific and their impact on the Northern Hemisphere summer circulation. *J. Meteor. Soc. Japan*, **65**, 373–390, https://doi.org/10.2151/jmsj1965.65.3_373.

Orsolini, Y. J., L. Zhang, D. H. W. Peters, K. Fraedrich, X. Zhu, A. Schneidereit, and B. van den Hurk, 2015: Extreme precipitation events over north China in August 2010 and their link to eastward-propagating wave-trains across Eurasia: Observations and monthly forecasting. *Quart. J. Roy. Meteor. Soc.*, **141**, 3097–3105, https://doi.org/10.1002/qj.2594.

Osborne, J. M., M. Collins, J. A. Screen, S. I. Thomson, and N. Dunstone, 2020: The North Atlantic as a driver of summer atmospheric circulation. *J. Climate*, **33**, 7335–7351, https://doi.org/10.1175/JCLI-D-19-0423.1.

Park, C., S.-W. Son, and H. Kim, 2021a: Distinct features of atmospheric rivers in the early versus late East Asian summer monsoon and their impacts on monsoon rainfall. *J. Geophys. Res. Atmos.*, **126**, e2020JD033537, https://doi.org/10.1029/2020JD033537.

——, ——, and J.-H. Kim, 2021b: Role of baroclinic trough in triggering vertical motion during summertime heavy rainfall events in Korea. *J. Atmos. Sci.*, **78**, 1687–1702, https://doi.org/10.1175/JAS-D-20-0216.1.

Ren, X., D. Yang, and X. Yang, 2015: Characteristics and mechanisms of the subseasonal eastward extension of the South Asian high. *J. Climate*, **28**, 6799–6822, https://doi.org/10.1175/JCLI-D-14-00682.1.

Sampe, T., and S.-P. Xie, 2010: Large-scale dynamics of the meiyu-baiu rainband: Environmental forcing by the westerly jet. *J. Climate*, **23**, 113–134, https://doi.org/10.1175/2009JCLI3128.1.

Seo, K.-H., J.-H. Son, and J.-Y. Lee, 2011: A new look at Changma: Atmosphere (in Korean with English abstract). *Atmosphere*, **21**, 109–121, https://doi.org/10.14191/Atmos.2011.21.1.109.

——, ——, S.-E. Lee, T. Tomita, and H.-S. Park, 2012: Mechanisms of an extraordinary East Asian summer monsoon event in July 2011. *Geophys. Res. Lett.*, **39**, L05704, https://doi.org/10.1029/2011GL050378.

Sohn, B. J., G.-H. Ryu, H.-J. Song, and M.-L. Oh, 2013: Characteristic features of warm-type rain producing heavy rainfall over the Korean peninsula inferred from TRMM measurements. *Mon. Wea. Rev.*, **141**, 3873–3888, https://doi.org/10.1175/MWR-D-13-00075.1.

Stuecker, M. F., A. Timmermann, F.-F. Jin, S. McGregor, and H.-L. Ren, 2013: A combination mode of the annual cycle and the El Niño/Southern Oscillation. *Nat. Geosci.*, **6**, 540–544, https://doi.org/10.1038/ngeo1826.

——, F.-F. Jin, A. Timmermann, and S. McGregor, 2015: Combination mode dynamics of the anomalous Northwest Pacific anticyclone. *J. Climate*, **28**, 1093–1111, https://doi.org/10.1175/JCLI-D-14-00225.1.

Takaya, K., and H. Nakamura, 2001: A formulation of a phase-independent wave-activity flux for stationary and migratory quasigeostrophic eddies on a zonally varying basic flow. *J. Atmos. Sci.*, **58**, 608–627, https://doi.org/10.1175/1520-0469(2001)058<0608:AFOAPI>2.0.CO;2.

Takaya, Y., I. Ishikawa, C. Kobayashi, H. Endo, and T. Ose, 2020: Enhanced meiyu–baiu rainfall in early summer 2020: Aftermath of the 2019 super IOD event. *Geophys. Res. Lett.*, **47**, e2020GL090671, https://doi.org/10.1029/2020GL090671.

Tziperman, E., M. A. Cane, S. E. Zebiak, Y. Xue, and B. Blumenthal, 1998: Locking of El Niño's peak time to the end of the calendar year in the delayed oscillator picture of ENSO. *J. Climate*, **11**, 2191–2199, https://doi.org/10.1175/1520-0442(1998)011<2191:LOENOS>2.0.CO;2.

Wu, Z., B. Wang, J. Li, and F.-F. Jin, 2009: An empirical seasonal prediction model of the East Asian summer monsoon using ENSO and NAO. *J. Geophys. Res.*, **114**, D18120, https://doi.org/10.1029/2009JD011733.

Xie, S.-P., H. Annamalai, F. A. Schott, and J. P. McCreary, 2002: Structure and mechanisms of South Indian Ocean climate variability. *J. Climate*, **15**, 864–878, https://doi.org/10.1175/1520-0442(2002)015<0864:SAMOSI>2.0.CO;2.

——, K. Hu, J. Hafner, H. Tokinaga, Y. Du, G. Huang, and T. Sampe, 2009: Indian Ocean capacitor effect on Indo-western Pacific climate during the summer following El Niño. *J. Climate*, **22**, 730–747, https://doi.org/10.1175/2008JCLI2544.1.

——, Y. Kosaka, Y. Du, K. Hu, J. S. Chowdary, and G. Huang, 2016: Indo-western Pacific Ocean capacitor and coherent climate anomalies in post-ENSO summer: A review. *Adv. Atmos. Sci.*, **33**, 411–432, https://doi.org/10.1007/s00376-015-5192-6.

Xiong, Z., S. Wang, Z. Zeng, and C. Fu, 2003: Analysis of simulated heavy rain over the Yangtze River Valley during 11–30 June 1998 using RIEMS. *Adv. Atmos. Sci.*, **20**, 815–824, https://doi.org/10.1007/BF02915407.

Xu, P., L. Wang, and W. Chen, 2019: The British–Baikal Corridor: A teleconnection pattern along the summertime polar front jet over Eurasia. *J. Climate*, **32**, 877–896, https://doi.org/10.1175/JCLI-D-18-0343.1.

Yamaura, T., and T. Tomita, 2011: Spatiotemporal differences in the interannual variability of Baiu frontal activity in June. *Int. J. Climatol.*, **31**, 57–71, https://doi.org/10.1002/joc.2058.

Yokoyama, C., H. Tsuji, and Y. N. Takayabu, 2020: The effects of an upper-tropospheric trough on the heavy rainfall event in July 2018 over Japan. *J. Meteor. Soc. Japan*, **98**, 235–255, https://doi.org/10.2151/jmsj.2020-013.

Zhang, W., Z. Huang, F. Jiang, M. F. Stuecker, G. Chen, and F.-F. Jin, 2021: Exceptionally persistent Madden-Julian Oscillation activity contributes to the extreme 2020 East Asian summer monsoon rainfall. *J. Geophys. Res. Atmos.*, **48**, e2020GL091588, https://doi.org/10.1029/2020GL091588.

Zhou, Z.-Q., S.-P. Xie, and R. Zhang, 2021: Historic Yangtze flooding of 2020 tied to extreme Indian Ocean conditions. *Proc. Natl. Acad. Sci. USA*, **118**, e2022255118, https://doi.org/10.1073/pnas.2022255118.